

In the format provided by the authors and unedited.

Emergence of quantum correlations from interacting fibre-cavity polaritons

Guillermo Muñoz-Matutano ^{1,2,7*}, Andrew Wood^{1,2,7}, Mattias Johansson^{1,2,7}, Xavier Vidal ^{1,2}, Ben Q. Baragiola ^{1,2,3}, Andreas Reinhard^{1,2}, Aristide Lemaître ⁴, Jacqueline Bloch⁴, Alberto Amo ⁵, Gilles Nogues⁶, Benjamin Besga^{1,2,6}, Maxime Richard ^{1,6} and Thomas Volz ^{1,2*}

¹Department of Physics and Astronomy, Macquarie University, Sydney, New South Wales, Australia. ²ARC Centre of Excellence for Engineered Quantum Systems, Macquarie University, Sydney, New South Wales, Australia. ³ARC Centre for Quantum Computation and Communication Technology, School of Science, RMIT University, Melbourne, Victoria, Australia. ⁴Centre de Nanosciences et de Nanotechnologies, CNRS (C2N), Universities Paris-Sud and Paris-Saclay, Palaiseau, France. ⁵Univ. Lille, CNRS, UMR 8523, PhLAM - Physique des Lasers Atomes et Molécules, Lille, France. ⁶Univ. Grenoble Alpes, CNRS, Grenoble INP, Institut Néel, Grenoble, France. ⁷These authors contributed equally: Guillermo Muñoz-Matutano, Andrew Wood, Mattias Johansson. *e-mail: guillermo.munozmatutano@mq.edu.au; thomas.volz@mq.edu.au

Supplementary Information

Emergence of quantum correlations from interacting fiber-cavity polaritons

Guillermo Muñoz-Matutano^{1,2,†}, Andrew Wood^{1,2,†}, Mattias Johansson^{1,2,†}, Xavier Vidal^{1,2}, Ben Q. Baragiola^{1,2,3}, Andreas Reinhard^{1,2}, Aristide Lemaître⁴, Jacqueline Bloch⁴, Alberto Amo⁵, Gilles Nogues⁶, Benjamin Besga^{1,2,6}, Maxime Richard⁶, and Thomas Volz^{1,2,*}

¹ *Department of Physics and Astronomy, Macquarie University, NSW 2109, Australia*

² *ARC Centre of Excellence for Engineered Quantum Systems, Macquarie University, NSW 2109, Australia*

³ *Centre for Quantum Computation and Communication Technology, School of Science, RMIT University, Melbourne, Victoria 3001, Australia*

⁴ *Centre de Nanosciences et de Nanotechnologies, CNRS, Univ. Paris-Sud, Université Paris-Saclay, C2N-Marcoussis, 91460 Marcoussis, France*

⁵ *Univ. Lille, CNRS, Physique des Lasers Atomes et Molécules, F-59000 Lille, France*

⁶ *Univ. Grenoble Alpes, CNRS, Grenoble INP, Institut Néel, 38000 Grenoble, France*

† *These authors have equally contributed to this work*

* *thomas.volz@mq.edu.au*

1. THEORETICAL MODEL

The starting point for our model is a quantum well exciton coupled to a planar microcavity photon mode. The non-dissipative dynamics of such a system are governed by a Hamiltonian given by¹

$$\begin{aligned}
H = & \int d\mathbf{x} \sum_{i,j \in \{X,C\}} \hat{\Psi}_i^\dagger(\mathbf{x}) h_{i,j}^0 \hat{\Psi}(\mathbf{x}) \\
& + \frac{\hbar\kappa}{2} \int d\mathbf{x} \hat{\Psi}_X^\dagger(\mathbf{x}) \hat{\Psi}_X^\dagger(\mathbf{x}) \hat{\Psi}_X(\mathbf{x}) \hat{\Psi}_X(\mathbf{x}) \\
& + \frac{\hbar\Omega_R}{n_{\text{sat}}} \int d\mathbf{x} \hat{\Psi}_C^\dagger(\mathbf{x}) \hat{\Psi}_X^\dagger(\mathbf{x}) \hat{\Psi}_X(\mathbf{x}) \hat{\Psi}_C(\mathbf{x}) + H.c. \\
& + \hbar \int d\mathbf{x} F_p(\mathbf{x}, t) e^{-i\omega_p t} \hat{\Psi}_C^\dagger(\mathbf{x}) + H.c.
\end{aligned} \tag{1}$$

Here $\hat{\Psi}_{C,X}$ are the spatially-dependent quantum field annihilation operators that describe excitons (X) and cavity photons (C) and the kinetic energy term of the planar microcavity is given by

$$h^0 = \hbar \begin{pmatrix} \omega_X(-i\nabla) & \Omega_R \\ \Omega_R & \omega_C(-i\nabla) + V_C(\mathbf{x}) \end{pmatrix} \tag{2}$$

where $V_C(\mathbf{x})$ is the photon confining potential and $\hbar\omega_C$ and $\hbar\omega_X$ are the photon and exciton energies respectively. Ω_R is the vacuum Rabi frequency, giving the coupling rate between photons and excitons. There are two nonlinearities in the system: The first is a due to Coulomb-mediated interaction between excitons with a coupling rate κ ; the second one is due to the exciton oscillator strength saturation at high density, characterized by n_{sat} . The photonic pumping term is given by F_p and is assumed to be monochromatic with a frequency ω_p .

In the case of strong photonic confinement, the only relevant modes are the fundamental cavity photon mode with spatial wavefunction $\phi_C(\mathbf{x})$ and the exciton mode with the same spatial shape¹. This simplifies the Hamiltonian (1) to

$$\begin{aligned}
H = & \hbar\omega_X b^\dagger b + \hbar\omega_C a^\dagger a + \hbar\Omega_R (b^\dagger a + b a^\dagger) \\
& + \frac{\hbar\omega_{\text{nl}}}{2} b^\dagger b^\dagger b b - \hbar\alpha_{\text{sat}} \Omega_R (b^\dagger b^\dagger a b + a^\dagger b^\dagger b b) \\
& + \hbar\mathcal{F}(t) e^{-i\omega_p t} a^\dagger + \hbar\mathcal{F}^*(t) e^{i\omega_p t} a
\end{aligned} \tag{3}$$

where a and b are bosonic annihilation operators of the cavity photon mode and the exciton mode respectively. The effective photon drive strength \mathcal{F} , and effective nonlinearities α_{sat} and ω_{nl} are given by $\mathcal{F}(t) = \int d\mathbf{x} F_p(\mathbf{x}, t) \phi_C^*(\mathbf{x})$, $\alpha_{\text{sat}} = \int d\mathbf{x} |\phi_C(\mathbf{x})|^4 / n_{\text{sat}}$, and $\omega_{\text{nl}} = \kappa \int d\mathbf{x} |\phi_C(\mathbf{x})|^4$.

Finally, we note that the saturation parameter is negligible for typical microcavity parameters² and go into the interaction picture to remove the bare photon and exciton energies. This yields the effective Hamiltonian

$$H_{\text{eff}} = \hbar \Delta \omega_X b^\dagger b + \hbar \Delta \omega_C a^\dagger a + \hbar \Omega_R (b^\dagger a + a^\dagger b) + \frac{\hbar \omega_{\text{nl}}}{2} b^\dagger b^\dagger b b + \hbar \mathcal{F}(t) (a^\dagger + a) \quad (4)$$

where without loss of generality we have taken $\mathcal{F}(t)$ to be real and defined the detunings $\Delta \omega_C = \omega_C - \omega_p$ and $\Delta \omega_X = \omega_X - \omega_p$. In order to make contact with the experimental parameters Δ and Δ_{LP} used in the main text, we note that $\Delta \omega_C = \Delta/2 - \Delta_{LP} + \sqrt{\Omega_R^2 + \Delta^2/4}$ and $\Delta \omega_X = \Delta \omega_C - \Delta$. The Hamiltonian (4) describes a system consisting of a single-mode photon field (a) and a single-mode exciton field (b). The two fields are coupled with a Rabi frequency Ω_R , and the exciton field has a self-coupling nonlinearity with strength ω_{nl} . The photon field has a time-dependent drive $\mathcal{F}(t)$ which is related to the laser power via $\mathcal{F}(t) = \sqrt{P(t)\gamma_C/\hbar\omega_p}$ where $P(t)$ is the input power into the cavity mode and γ_C is the optical cavity decay rate.

In order to study the cavity dynamics and photon correlation functions it is also necessary to include dissipation and loss. This requires a master equation description of the system. We denote the density matrix of the system by $\rho(t)$, and introduce losses γ_C and γ_X , corresponding to the homogeneous linewidths of the photons and excitons respectively, resulting in a master equation for the system given by

$$\frac{d\rho}{dt} = \frac{i}{\hbar} [\rho, H_{\text{eff}}] + \frac{\gamma_C}{2} (2a\rho a^\dagger - a^\dagger a\rho - \rho a^\dagger a) + \frac{\gamma_X}{2} (2b\rho b^\dagger - b^\dagger b\rho - \rho b^\dagger b). \quad (5)$$

Due to the fact that the photonic driving term describes a Gaussian pulse rather than continuous excitation, we must find the full time-dependent solution to (5) and not merely find the steady state solution. To do this we treat the master equation as a time-dependent matrix differential equation, and numerically solve it in a tensor product Fock basis for the operators a and b . We truncate the basis by limiting the number of excitations in both the photon and exciton modes. For parameters describing our experiment, we found that an acceptable cutoff was between five and eight excitations in each mode depending on laser power.

Given the time-dependent solution $\rho(t)$, it is possible to use the quantum regression theorem to find two-time correlation values. For example, the two-time second-order coherence function for

the photon field is given by:

$$G^{(2)}(t, t') = \text{Tr} \left(a U(t, t') \left[a \rho(t') a^\dagger \right] a^\dagger \right) \quad (6)$$

and the normalized version by:

$$g^{(2)}(t, t') = \frac{\text{Tr} \left(a U(t, t') \left[a \rho(t') a^\dagger \right] a^\dagger \right)}{\text{Tr} \left(a \rho(t) a^\dagger \right) \text{Tr} \left(a \rho(t') a^\dagger \right)} \quad (7)$$

where $U(t, t')$ is the evolution superoperator that acts on the density matrix as $\rho(t) = U(t, t') \rho(t')$. However, we note that the experiment does not find the actual function $g^{(2)}(t, t')$ within the laser pulse, as the pulse width is shorter than the time resolution of the detectors used. Rather, over many pulses, the experiment registers all possible coincidences between t and t' and bins them together. In this situation the correct quantity to compare to experiment is³

$$\bar{g}^{(2)}(0) = \frac{2 \int_{-T}^T dt_1 \int_{t_1}^T dt_2 G^{(2)}(t_1, t_2)}{\int_{-T}^T dt_1 \int_{-T}^T dt_2 I(t_1) I(t_2)} \quad (8)$$

where the limits $(-T, T)$ encompass the full duration of each pulse, and $I(t) = \text{Tr} [\rho(t) a^\dagger a]$ is the average photon flux at time t . It is this quantity $\bar{g}^{(2)}(0)$ that is used in the main text when comparing the experimental results to the theoretical model.

2. POLARITON-POLARITON INTERACTIONS

As mentioned previously, the polaritonic nonlinearity can be traced back to the exciton-exciton exchange interaction $\hbar\kappa$ (in units of $\text{meV} \cdot \mu\text{m}^2$) in a quantum well^{1,4,5}. In a laterally confined mode, this interaction is enhanced by the forced proximity of the excitons into $\hbar\omega_{NL} = \hbar\kappa \times \int dx dy |\varphi_X(x, y)|^4$, where $\varphi_X(x, y)$ is the normalized excitonic in-plane wavefunction, and $A^{-1} = \int dx dy |\varphi_X(x, y)|^4$ is an inverse area that characterizes this enhanced overlap¹. For polaritons in a cavity with lateral confinement, and under resonant excitation into the lower polariton state, the polaritonic wavefunction is imposed by the photonic confinement, and in the strong coupling regime, it is linearly related to the excitonic wavefunction by the Hopfield coefficient C_x . As a result, the polaritonic nonlinearity can be derived from the excitonic one as $U = \hbar\kappa |C_x|^4 \times A^{-1} = \hbar\omega_{NL} |C_x|^4$ (in units of meV), and $\hbar g = \hbar\kappa |C_x|^4 = \hbar\omega_{NL} |C_x|^4 \times A$ (in units of $\text{meV} \cdot \mu\text{m}^2$).

As discussed in the main text, when determining the exciton-exciton nonlinearity in our experiment, the best fit is obtained for a confinement-enhanced exciton-exciton interaction constant

$\hbar\omega_{NL} = 0.018 \pm 0.010$ meV. To obtain a more generic polariton-polariton interaction strength $\hbar g$ it is necessary to scale $\hbar\omega_{NL}$ by the mode overlap between the photonic cavity mode and the exciton wavefunction. Using a finite element calculation of the whole structure (see Section 6), we find that the mode is Gaussian with a waist size $w_0 = 1.17 \mu\text{m}$ (see SI). In this case, $\hbar g = \hbar\omega_{NL}|C_x|^4\pi w_0^2$, using the scaling area πw_0^2 . With an excitonic fraction $|C_x|^2 = 51\%$ this analysis yields $\hbar g = 0.020 \pm 0.011$ meV $\cdot\mu\text{m}^2$. The confidence of this value is illustrated by the plot in Figure 4c in the main text that shows the coefficient of determination $R^2(\hbar g)$ of the theoretical fit to our data. $R^2(\hbar g)$ exhibits a clear maximum for $g = g_0$, as well as a peaked structure from which the uncertainty is well-defined. The associated exciton-exciton interaction strength $\hbar\kappa = 0.076 \pm 0.042$ meV $\cdot\mu\text{m}^2$.

3. PULSE SHAPING

Tuning the time duration of the excitation pulse is of critical importance in achieving polariton blockade and obtaining stronger quantum correlations.

The better antibunching is due to the blockade becoming more effective as the spectral width of the pulse shrinks below the nonlinear energy shift imparted due to the presence of a second polariton. The shift in the minimum is beneficial as it moves the peak $g^{(2)}(0)$ antibunching into the region where there is better signal (i.e. more counts due to being near resonance), enhancing the signal to noise ratio of the measurement.

This is illustrated in Figure S.1.b, which shows an energy diagram with two different pulsed excitation conditions. (1) corresponds to a situation where $\delta_L > \tau_{LP}$, so that the spectral width of the pulse is less than γ_{LP} . (2) corresponds to the opposite situation, where $\delta_L \leq \tau_{LP}$, so the pulse spectral width is on the order of or greater than γ_{LP} . This results in a compressed (1) or expanded (2) excitation laser range ($\delta(\Delta_{LP})$) where the antibunching / bunching photon statistics are observed.

Experimentally, the excitation pulses are generated by a picosecond Ti:sapphire laser. These pulses are too short as compared to γ_{LP} and thus need to be reshaped. They are sent into a monochromator through an iris of variable diameter, which controls the input numerical aperture, and hence the spectral resolution at the output slit. The pulse length could thus be adjusted between 15 ps and 50 ps as is shown by a characterization with a streak camera (Figure S.2).

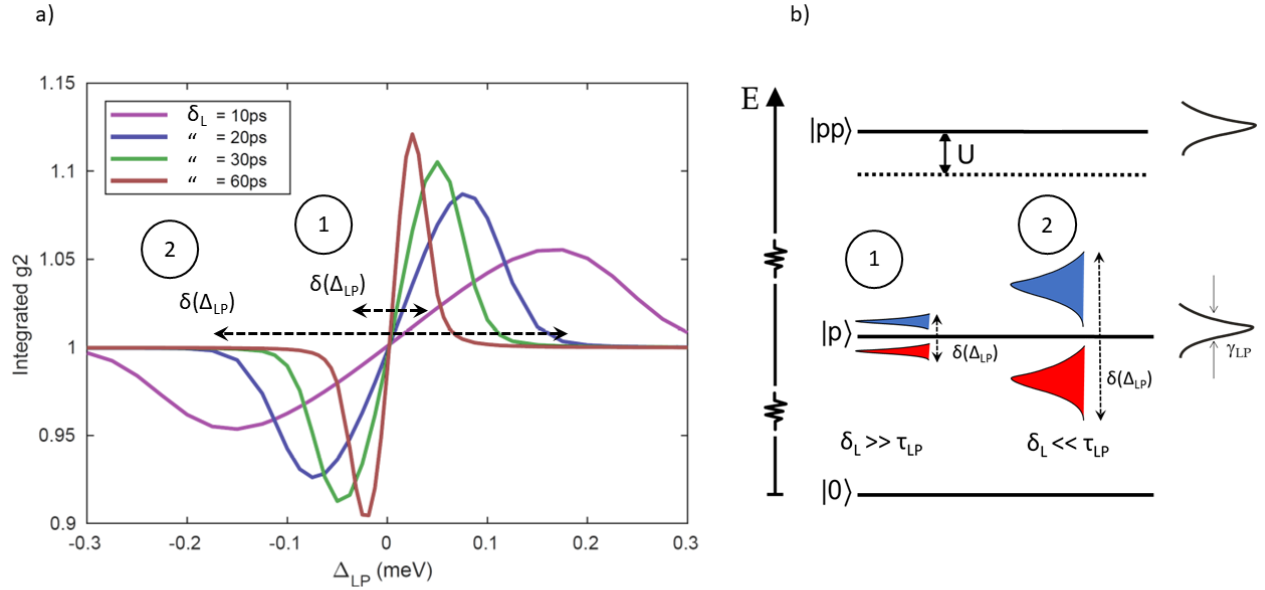


FIG. S.1. **Effect of pulse width on the correlations.** a) Calculated $g^{(2)}(0, \Delta_{LP})$ for different excitation pulse duration $\delta_L = 10, 20, 30$ and 60 ps. b) Schematic representation of the polariton excitation ladder. The pulse width is shown for comparison with the polariton linewidth γ_{LP} and the blueshift U . Label "1" refers to the case where the pulse duration is longer than the lower polariton lifetime; and "2", where the pulse duration is shorter than or similar to the lower polariton lifetime.

4. NEGATIVELY CHARGED TRION AS A LOSS CHANNEL FOR POLARITONS

As explained in the main text, photoluminescence (PL) spectra of the polariton states under non-resonant excitation at 825 nm show a small but distinct spectral feature approximately 1.2 meV red detuned from the bare exciton (X^0) resonance which can be seen in Figure S.3. A similar feature has been reported before in fiber based cavity experiments⁶ and has been interpreted as an impurity resonance in the semiconductor. However, owing to its spectral properties, this feature better agrees with the negative trion state (X^{-1})⁷.

This trion resonance plays an important role as energy-dependent source of loss and decoherence for polaritons that will be key for understanding the results of our correlation measurements. To quantify this trion-induced loss mechanism, we now develop a simple theoretical model treating the trion resonance as additional irreversible loss channel⁸ in order to estimate the overall lifetime

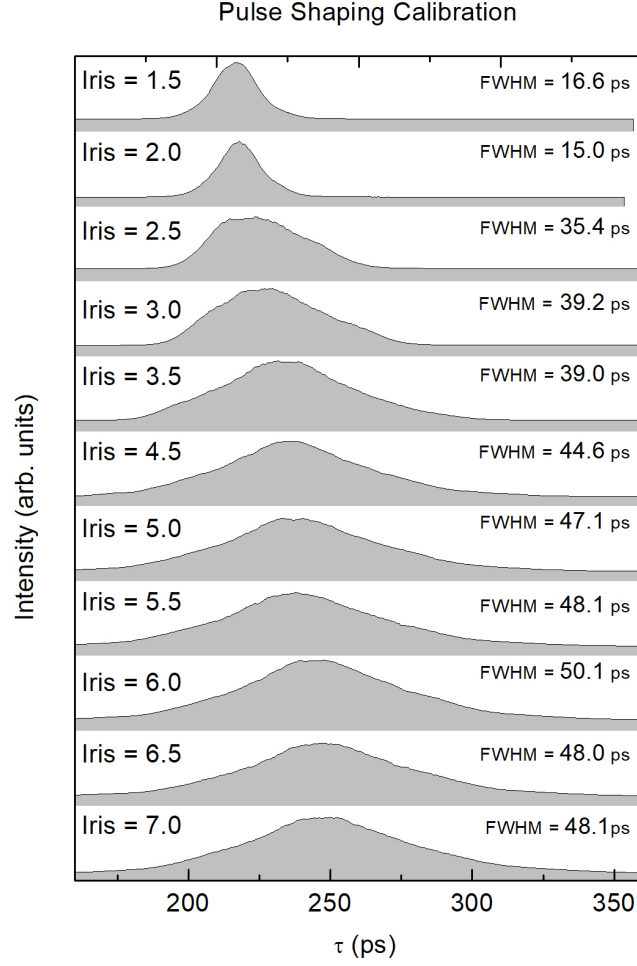


FIG. S.2. **Measured laser pulse duration.** Streak camera characterization of the pulses duration tuned by the pulse shaper.

dependence on Δ . This loss channel constitutes an additional source of noise that shows up in the measured correlations.

We model the polariton decay time τ_{LP} as the sum of two energy dependent contributions:

$$\frac{1}{\tau_{LP}(E_{LP})} = \frac{1 - |C_X(E_{LP})|^2}{\tau_C} + |C_X(E_{LP})|^2 \gamma_T(E_{LP}) \quad (9)$$

where $C_X(E_{LP})$ is the excitonic Hopfield coefficient, and τ_C is the bare cavity lifetime. The first term is the "usual" polariton loss channel throughout the cavity mirrors. $\gamma_T(E_{LP})$ describes the irreversible elastic scattering of a polariton into the trion density of states. Within a Fermi golden rule approach, this mechanism is proportional to the trion density of state at the polariton energy

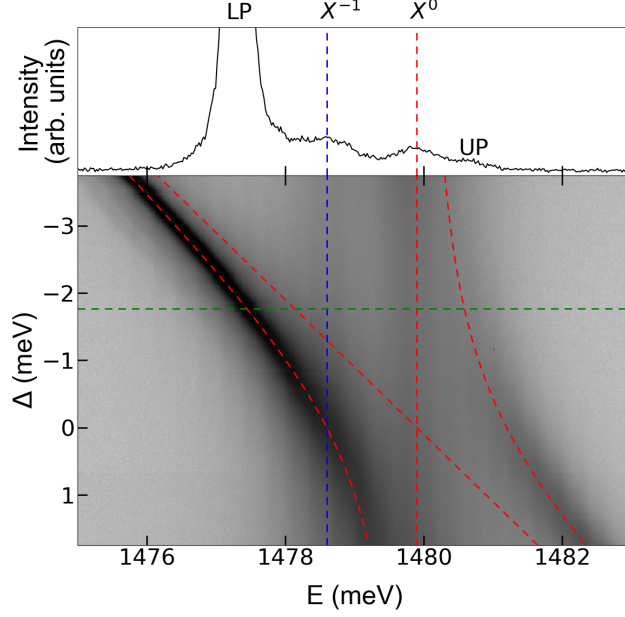


FIG. S.3. **Photoluminescence (PL) under non-resonant excitation at 825nm.** The PL intensity is color-coded from white (dim) to black (bright). The black anti-crossing lines are the upper and lower polariton modes. The black dotted lines show the neutral exciton (X^0) and negative trion (X^{-1}) states. The top spectrum is a slice in this map, taken for a slightly negative detuning, shown by the red solid line. The X^{-1} state is found ~ 1.2 meV red detuned from the neutral exciton state.

E_{LP} . We assume for simplicity that the latter takes a Gaussian shape such that

$$\gamma_T(E_{LP}) = S \exp\left(-[E_{LP} - E_X - E_B]^2 / 2\sigma_T^2\right), \quad (10)$$

where S is the characteristic scattering rate, $E_X - E_B$ is the trion transition energy in terms of the neutral exciton energy minus the binding energy, and σ_T is the trion linewidth. All the parameters in this model are known from photoluminescence measurement of the lower polariton and trion state (see inset in Fig. S.4b), except for S , and within a small range, τ_C .

In order to include the effect of this additional loss channel into the master equation model, we define an effective excitonic lifetime as:

$$\frac{1}{\tau_X^{\text{eff}}} = \gamma_T. \quad (11)$$

Following this definition we include τ_X^{eff} as a parameter in the master equation model described above, identifying $\gamma_X = \gamma_T$, which encompasses all forms of excitonic loss. This effective parameter varies with Δ , and is calculated via Eqs. (9) – (10).

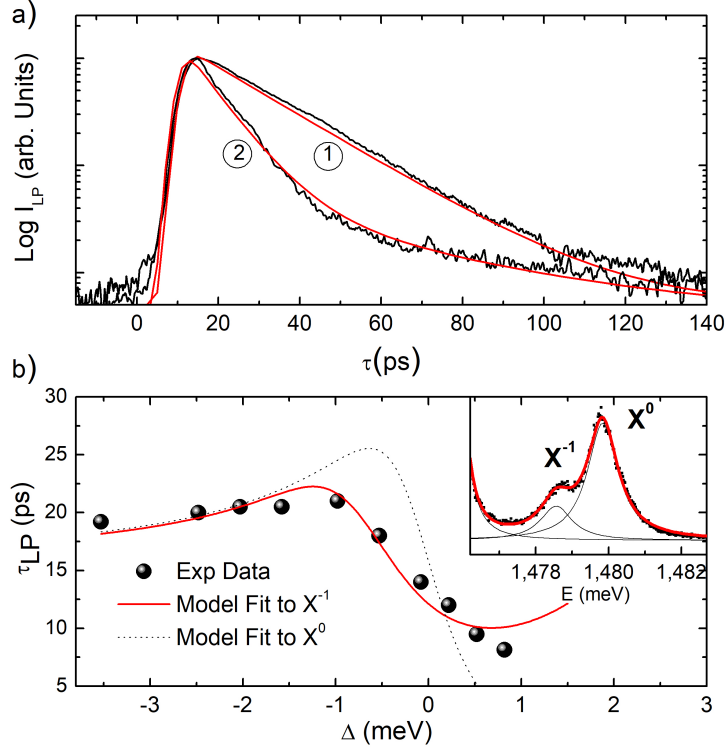


FIG. S.4. **Polariton decay time.** a) Experimental LP lifetime decay curve recorded at $\Delta = -3.53$ meV (labelled "1") and $\Delta = +0.82$ meV (labelled "2"). Red discontinuous lines corresponds to fits based on a single exponential decay (1) and on a bi-exponential decay (2), respectively. b) Experimentally measured Lower Polariton (LP) decay time measured under resonant excitation vs Δ (black dots). The data are compared with a two-coupled-oscillator model that includes polariton losses by elastic scattering into the negative trion X^{-1} density of states (solid red line), or by elastic scattering into the disordered neutral exciton density of states (dashed line). Inset: Photoluminescence spectra under non-resonant excitation at 1.503eV. Black lines are Lorentzian fits of the neutral exciton and negative trion.

To obtain a numerical estimate of this effective excitonic lifetime, we performed lifetime measurements of the polariton modes under resonant excitation for different Δ . Figure S.4 shows $\tau_{LP}(E_{LP})$ data as obtained from time resolved decay measurement of the polariton state under resonant excitation. When the lower polariton mode is tuned far away on the red side of the trion resonance, the polariton decay is monoexponential in time as shown in Fig. S.4a, and the characteristic lifetime is well accounted for by taking into account the bare cavity lifetime and the excitonic fraction. In this approximation, the lifetime is expected to increase for increasing Δ , consistent with our

observations up to $\Delta \simeq -1$ meV. For larger Δ , however, as the polariton mode approaches the trion resonance, the trion starts to provide a second loss channel in addition to the direct photon loss through the cavity. In this regime, the decay becomes bi-exponential (Fig. S.4a) and the polariton lifetime sharply decreases for increasing Δ . On resonance with the trion ($\Delta \simeq 0.6$ meV) this additional loss channel dominates⁹, and exceeds the cavity losses by a factor ~ 2 . The fast part of the bi-exponential decay curve corresponds to the polariton decay with $\tau_{LP} \approx 8$ ps, including both the cavity decay and irreversible loss into the large trionic density of states. The slow decay can be attributed to re-emission from the trion resonance into the polariton mode with a characteristic time of ≈ 65 ps. The solid red line in Figure S.4b is a fit using the aforementioned model showing very good agreement, allowing us to extract the bare cavity lifetime $\tau_C = 16$ ps, and a trion-mediated characteristic loss rate of $S = 0.134$ ps⁻¹. Interestingly, if we neglect the trion contribution and replace it with losses into a localized neutral exciton density of state by setting E_B to zero and set σ_T to σ_X , we cannot fit the data in a convincing way (dashed line).

We note that our theory model does not explicitly include a quantitative description of how photon correlations are affected by the trion resonance or the neighboring polariton mode π_Y , as this would require new theoretical developments that clearly go beyond the scope of the present paper. Instead, in order to better facilitate the comparison between experiment and theory, we determine the range of validity of the model. In order to do so, in the main text we used a quantity $\tilde{T}(\Delta_{LP})$ which parameterizes the accuracy of our model at a given $\tilde{T}(\Delta_{LP})$, which we now define.

We take $\tilde{T}(\Delta_{LP}) = T_X(\Delta_{LP})/[T_X(\Delta_{LP}) + T_Y(\Delta_{LP}) + T_{X^{-1}}(\Delta_{LP})]$, and as such it quantifies the fraction of laser light transmitted by the π_X polariton mode alone. It estimates the amount of perturbation this mode is subject to for a given Δ_{LP} , due to its spectral overlap with the other perturbing transitions. $T_X(\Delta_{LP})$, $T_Y(\Delta_{LP})$, and $T_{X^{-1}}(\Delta_{LP})$ are the contributions to the transmission spectra of the π_X and π_Y polariton modes, and of the trion resonance, respectively, determined from the transmission measurements. Hence, $\tilde{T} = 1$ means that the π_X polariton mode is unperturbed. For this ideal case, we expect the best possible agreement with the single-mode theory. The smaller \tilde{T} , the more the π_X polariton mode is perturbed, and the more the experiment is expected to depart from the single-mode theoretical expectation.

5. SECOND-ORDER ZERO-DELAY CORRELATION: DETERMINATION AND ERROR BARS

The avalanche photodetectors (APDs) that we used in this experiment have a time resolution of $\simeq 350$ ps. Since the polariton dynamics under resonant excitation is < 40 ps, we can reasonably assume that the correlations between two photons delayed by this timescale are equally spread over the whole measured zero-delay coincidence peak. On the other hand, it also means that since the other coincidence peaks are separated by an integer multiple of 13 ns (laser repetition period), they cannot feature any polariton correlations. Figure S.5 shows an extended raw two-photon coincidences histogram and the corresponding integrated coincidences histogram for our strongest antibunching in Figure 3c of the main text (data point (i)). Given the rather small contrast of the antibunching and the overall noise in the data, a careful statistical analysis is needed.

In order to maximize the statistical significance of our data, we chose to truncate the data of the zero delay peaks (centered at bin zero) at time bins $\pm W$, and hence reject the far edges of the peaks that which contain more dark coincidence counts from the APDs than actual signal. To determine the optimal W , we modeled the coincidence counts in each time bin j as being the sum of the signal S_j , the statistical noise related to the number of counts uncertainty and the dark coincidence counts. As a result the sum of the zero delay coincidences reads

$$A_0 = \sum_{j=-W}^W S_j, \quad (12)$$

and the corresponding signal-to-noise:

$$SNR(W) = \frac{\sum_{j=-W}^W S_j}{\sqrt{\sum_{j=-W}^W S_j + (2W + 1)S_D}}, \quad (13)$$

where S_D is the number of dark coincidence counts which is a constant over all bins (whether it is due to dark/dark, dark/signal or signal/dark coincidences). The signal to noise function (13) exhibits a maximum that depends on the parameters. Figure S.6 shows a typical raw zero delay correlation peak. A dark count of $S_D = 0.5$ counts per bin is found, and the Gaussian best fit of the peak exhibits a full width at half maximum of 600 ps and an amplitude of 95 counts in the central bin. With these parameters the largest signal-to-noise ratio is achieved for a truncation window of $2W = 896$ ps full width.

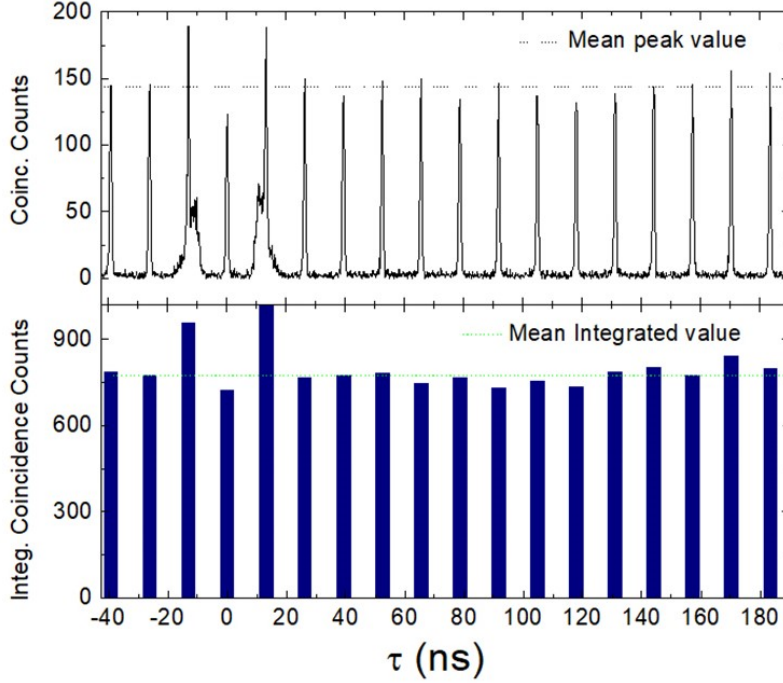


FIG. S.5. **Anti-bunched raw coincidence data and integrated coincidences histogram.** (upper panel) Extended coincidence counts histogram for the raw data displayed in Figure 3d of the main text. The mean peak value is indicated by a dotted black line. (lower panel) Integrated coincidences histogram (blue bars) extracted from the raw data by following the analysis protocol described in the text further below. The mean integrated value is indicated by the dotted green line.

$g^{(2)}(0) = \frac{A_0}{\langle A \rangle}$ is then determined as the ratio of the sum of the counts in the zero delay peak within the truncation window (A_0) and the average sum of the counts in the uncorrelated peaks within the same truncation window ($\langle A \rangle$). The experimental uncertainty on A_0 is derived from the measured standard deviation σ of A_k , the sum of the counts in the peak k (also truncated) where k runs over every peak of uncorrelated events (300 peaks in total). Then, according to the central limit theorem, the uncertainty over $\langle A \rangle$ is given by $\varepsilon(\langle A \rangle) = \frac{\sigma}{\sqrt{N_p}}$, where $N_p = 300$ is the number of peaks of uncorrelated events. We have also included two more corrections: subtraction of the noise correlations from the APD dark counts¹⁰ and the compensation of the slow long delay decay caused by the finite efficiency of the detectors and by the count rate of the APDs. Figure S.7 shows the $g^{(2)}(0)$ values obtained and their error bars after applying this method. It corresponds

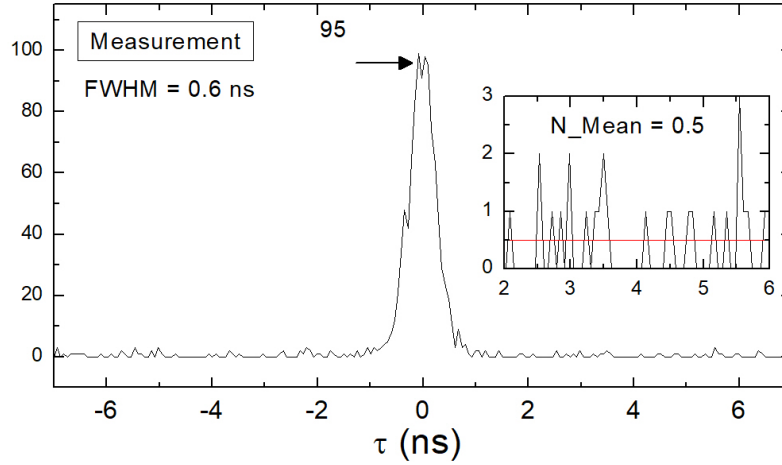


FIG. S.6. **Typical zero-delay raw coincidences peak.** The FWHM of the zero-delay peak is 0.6 ns, with a maximum of 95 coincidence counts. Dark coincidence counts from the detectors are delay independent, and amount here to 0.5 counts on average (Inset).

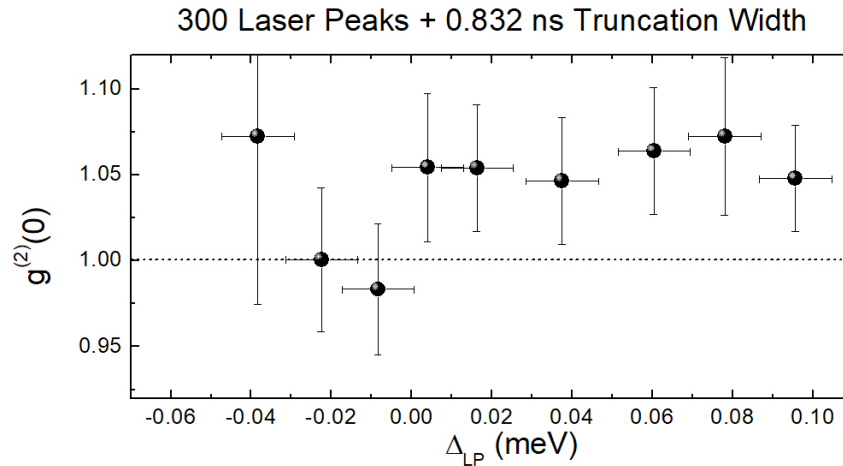


FIG. S.7. **Extracted second order autocorrelation function at zero time delay.** $g^{(2)}(0)$ values extracted following the analysis protocol described in the text.

to Figure 4.a of the main text.

In order to check the robustness of our method, we analyzed two values of $g^{(2)}(0)$ ($\Delta_{LP} = -0.010$ meV and $+0.037$ meV in Figure S.7), as a function of W and N_p , for $W = 0.512$ ns, 0.832 ns, 1.216 ns and 1.600 ns, and $n_p = 300, 100, 30$ and 10 peaks. Figure S.8 shows the result: As expected,

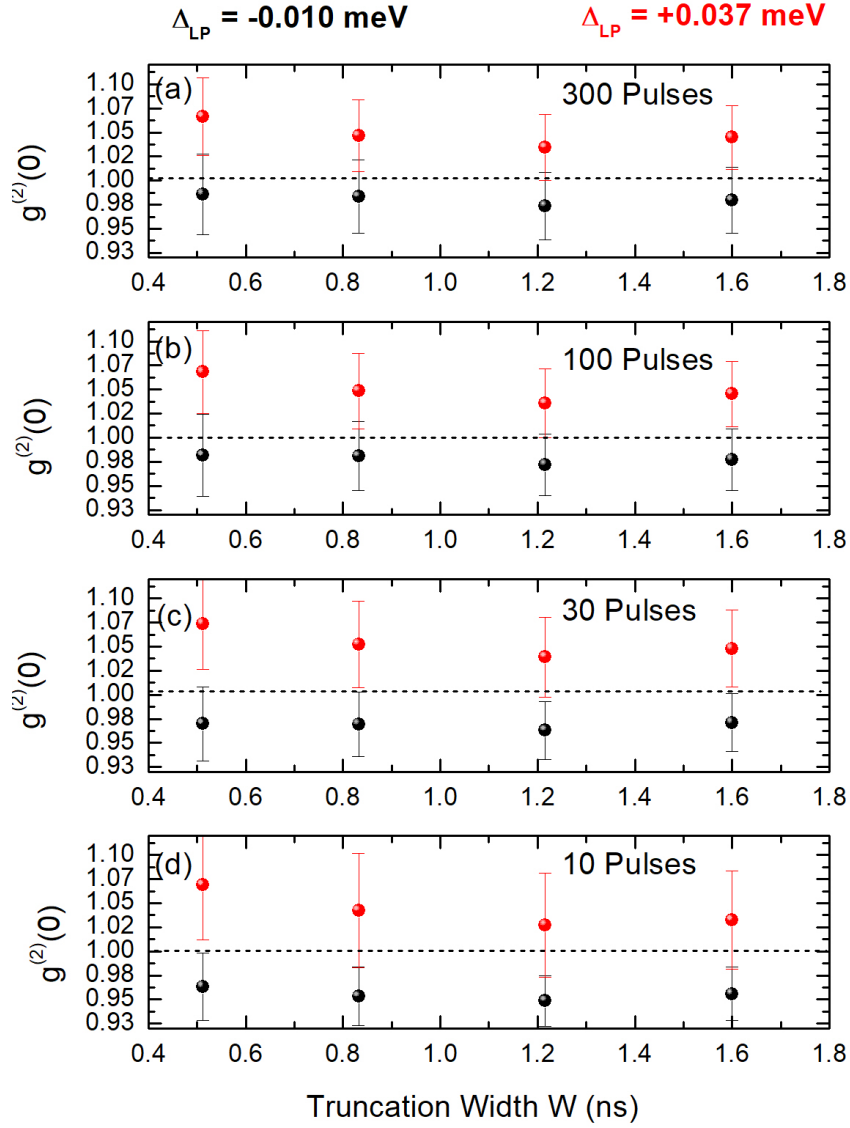


FIG. S.8. **Sensitivity of the result on the analysis parameters.** Values obtained for $g^{(2)}(0)$ (at $\Delta_{LP}) = -0.010$ meV and $+0.037$ meV in Figure S.8), from analysis of the raw data, using $W = \{0.512, 0.832, 1.216, 1.600\}$ ns, and $n_p = \{300, 100, 30, 10\}$ peaks.

accounting for the maximum number of peaks, plus a truncation width W chosen within this time interval maximizes the signal to noise ratio. Figure S.9 shows raw photon correlation measurement for both laser detunings until 11 consecutive correlated pulses.

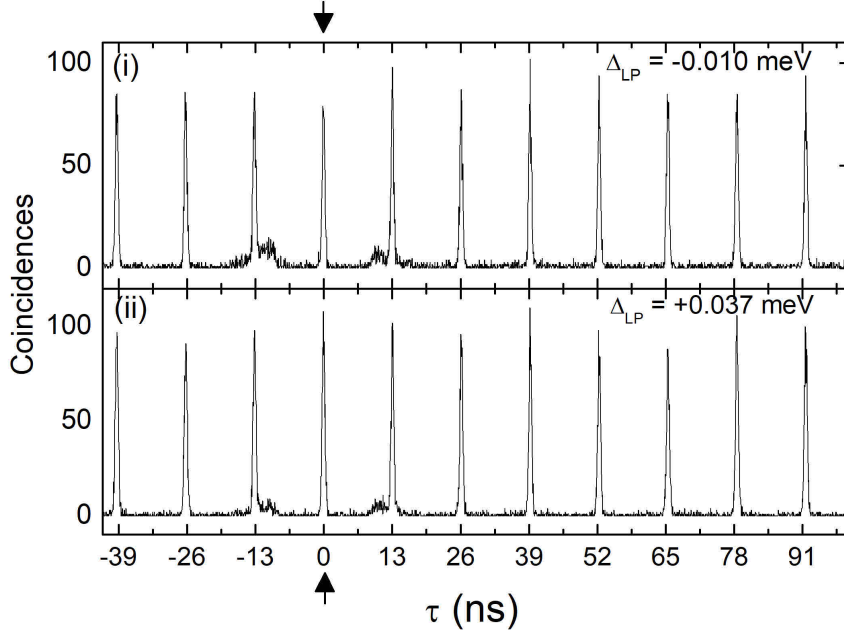


FIG. S.9. **Raw photon correlation histograms** (i) Raw photon correlation histogram from main text Figure 4.b with laser detuning $\Delta_{LP} = -0.010$ meV until 11 consecutive correlated pulses. (ii) Raw photon correlation histogram from main text Figure 4.b with laser detuning $\Delta_{LP} = +0.037$ meV until 11 consecutive correlated pulses. Arrows indicate the position of the zero delay peak.

6. FINITE ELEMENTS SIMULATION OF THE CAVITY MODE

We have calculated the exact shape of the polariton lowest transverse mode within the cavity volume by numerical simulations of Maxwell's equations, using the finite element software COMSOL. We assumed a circular symmetry around the axis z of the optical fiber. Taking into account the expected symmetries of the mode, the calculation is carried out in the r, z plane, with $r \geq 0$, and only for the in-plane components of the electric field $\mathbf{E} = (E_r, E_z)$. The simulations geometry is shown in Figure S.10 (a). The origin of the r, z space is taken at the interface between the MBE grown sample and the vacuum. Calculations are limited to the space defined by $0 \leq r \leq r_{\max}$ and $-z_{\min} \leq z \leq z_{\max}$, with $r_{\max} = 10 \mu\text{m}$ and z_{\min} and z_{\max} large enough so as to fully encompass the bottom and top DBR reflectors and a small portion of GaAs substrate and SiO₂ fiber. Before the top and bottom boundaries, a 300 nm-thick perfectly matched layer is used in order to absorb any outgoing wave without reflection. As a consequence one assumes a boundary condition $E = 0$ for $r = r_{\max}$, $z = z_{\max}$ and $z = -z_{\min}$. On the z axis, one assumes $E_z = 0$ (perfect electric conductor).

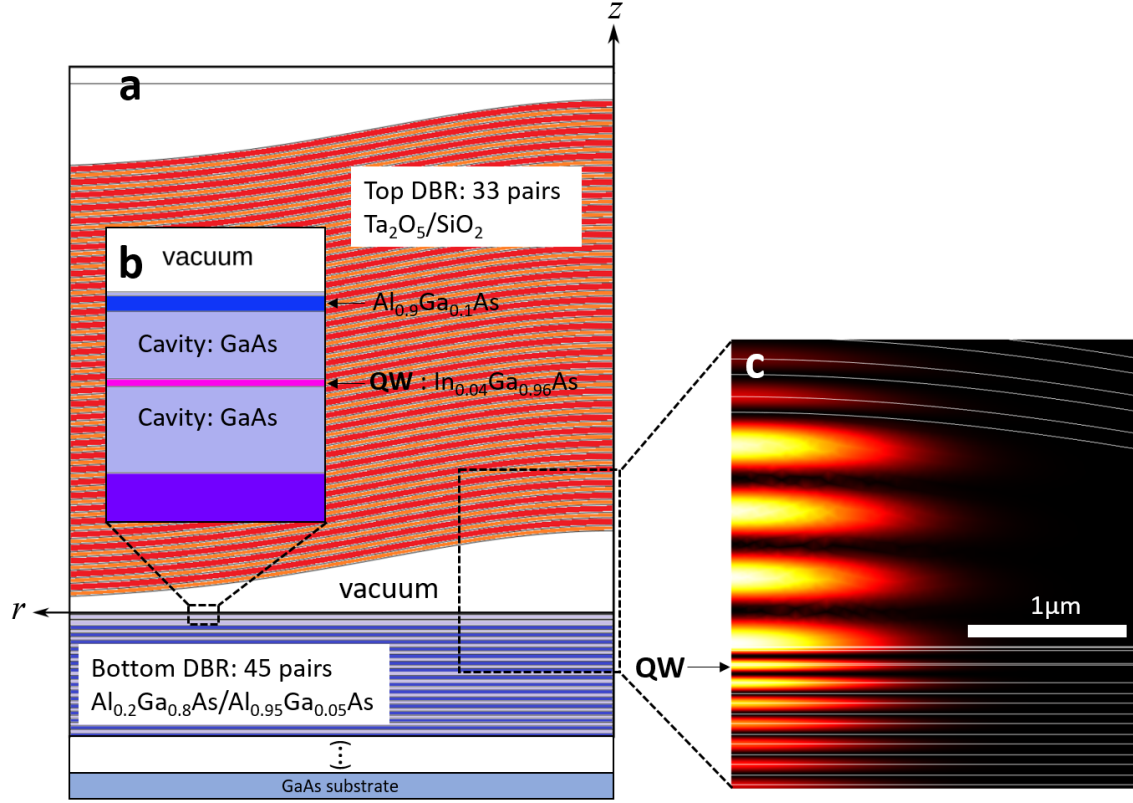


FIG. S.10. **Finite element analysis of the cavity mode.** (a) Sketch of the geometry used in the numerical simulation, the colors refer to a specific material. (b) is a zoom of the cavity geometry in the vicinity of the QW. (c) color-coded intensity map $I(r, z)$ of the fundamental transverse mode resonant with ω_x , the position of the QW is indicated by the arrow.

For the fiber DBR, we assumed that the coating is made of successive layers deposited by a directional method. As a consequence each interface is a replica of the initial profile etched on the fiber. the etched profile is measured to be of Gaussian form, which is what we use in the simulation: the interface between the final dielectric layer and the vacuum is taken as:

$$h(r) = h_{\text{fiber}} + \rho \times e^{-\frac{r^2}{2w_m^2}}.$$

Interferometric measurements of the fiber profile yield $\rho = 1.3 \mu\text{m}$ and a radius of curvature $R \simeq 13 \mu\text{m}$ at $r = 0$. Thus one has $w_m = \sqrt{\rho \times R} = 4.11 \mu\text{m}$. The low temperature refractive indices for $\text{Al}_x\text{Ga}_{1-x}\text{As}$, Ta_2O_5 and SiO_2 are taken from Refs.^{11,12} and¹³ respectively. The QW background index of refraction is assumed to be that of GaAs. This assumption has a negligible influence on the mode shape in real space.

The software searches for field eigenmodes of the form $\mathbf{E} = \hat{\mathbf{E}}(r, z)e^{-i\omega_c t}$ for the above described structure where ω_c is in the vicinity of $\omega_X = E_X/\hbar$. The calculated eigenfrequencies ω_c are complex numbers whose imaginary part reflects the losses of the corresponding mode. A fundamental transverse mode is found with $\omega_c \simeq \omega_X$ for $h_{\text{fiber}} = 205$ nm in good agreement with the experiments. Its Q factor ~ 30000 , which is limited by the absorption in the Ta₂O₅ layers and its value would be closer to the experimental value if one considered the absorption in the GaAs layers. Figure S.10(c) shows a 2D-map of its intensity distribution $I(r, z)$ in the region of interest. As expected, it presents an antinode at the QW layer (arrow). The intensity $I(z = z_{\text{QW}}, r)$ agrees with a gaussian function $I_0 e^{-2r^2/\omega_0^2}$, over several orders of magnitude, with $\omega_0 = 1.17 \mu\text{m}$.

7. PHOTON CORRELATION MEASUREMENT IN A SECOND CAVITY

We carried out a second set of photon correlation measurements in a second fiber cavity with different cavity parameters. While the radius of curvature for this cavity was similar to the previous one, the cavity lifetime of 8.3 ps was significantly shorter than for the other cavity. Figure S.11 a) displays the low-temperature photoluminescence (PL) map as a function of cavity detuning (Δ), obtained under non-resonant excitation (at $E_L = 1.55$ eV). The characteristic avoided crossing of the excitonic and photonic modes was observed, producing the Lower Polariton (LP) and Upper Polariton (UP) dressed states. We find a vacuum Rabi splitting of $2\hbar\Omega_R = 3.04$ meV, with slightly higher QW exciton energy ($E_X = 1480.65$ meV) than in the spot studied in the main text of the paper.

In order to evaluate the best Δ to carry out photon correlation measurements and to minimize the effect of the trion transition, we measured resonant transmission spectra in the close vicinity of $\Delta = 0$. Figure S.11 b) displays the evolution of the experimental LP linewidth (γ_{Exp}) (blue filled circles) and the calculated LP radiative linewidth (γ_{Rad}) (black filled squares) as a function of Δ . As displayed, at $\Delta \simeq -0.45$ meV both quantities start to diverge, as a consequence of the losses produced by the scattering with the trion transition.

As a second control parameter we calculated the following figure of merit ρ_0 :

$$\rho_0 = \frac{|C_X|^4 \sqrt{R_0}}{\gamma_{Exp}} \times f_P; \quad f_P = \frac{\gamma_{Rad}}{\gamma_{Exp}}; \quad R_0 = \frac{R_{Det}^2}{\theta} \quad (14)$$

where R_{Det} is the detector count rate and θ is the pulsed laser frequency. ρ_0 therefore measures the detector count rate versus the polariton linewidth promising the best signal-to-noise ratio for

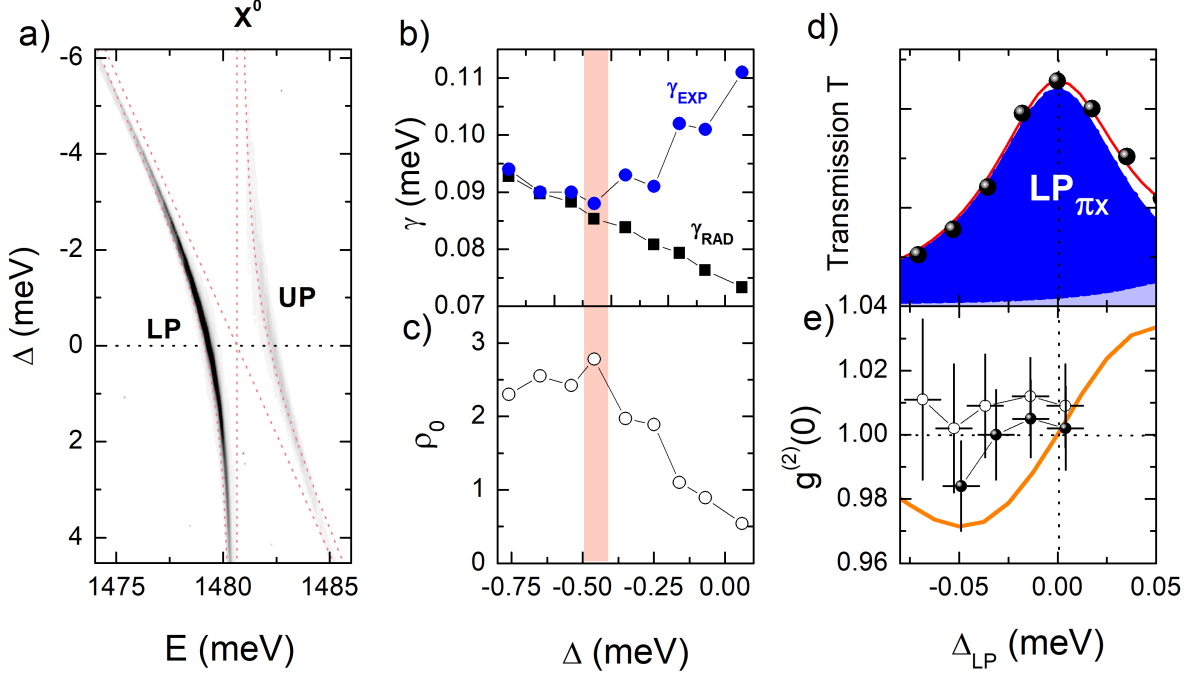


FIG. S.11. **Optical characterization and photon correlation measurement on a second fiber cavity**) Low-temperature photoluminescence (PL) map as a function of cavity detuning (Δ). b) Experimental LP linewidth (γ_{Exp}) (blue filled circles) and the calculated LP radiative linewidth (γ_{Rad}) (black filled squares) as a function of Δ . c) evolution of the figure of merit ρ_0 as a function of Δ . In both b) and c) figures $\Delta = -0.45$ meV (redish shadow) shows the best signal-to-noise ratio for the photon correlation measurements. d) Measured resonant transmission spectra of the the π_X LP transition (black dots), and Lorentzian fitting to both linear LP transitions (bluish shadows). Red continuous line represents the cumulative fit. e) Photon correlation measurements as a function of laser detuning (Δ_{LP}) for $\Delta = -0.45$ meV and two excitation powers: 700 pW (open circles) and 200 pW (filled circles).

the measurements at its maximum value. Figure S.11 c) shows the evolution of ρ_0 as a function of Δ , with $\Delta = -0.45$ meV corresponding to the position of its maximum. As both direct linewidth and ρ_0 criteria coincide, we have performed photon correlation measurements as a function of laser detuning (Δ_{LP}) for $\Delta = -0.45$ meV and two excitation powers. Figure S.11 e) shows the measured $g^{(2)}(0)$ value when scanning the low energy tail of the π_X LP transition (Figure S.11 d) with the excitation laser. Here we used two different average excitation powers: 700 pW (open circles) and 200 pW (filled circles). When using high excitation power, all measurements return $g^{(2)}(0) \geq 1$. However, when the excitation power is reduced to 200 pW, we find a clear minimum

$g^{(2)}(0) = 0.984 \pm 0.014 < 1$ at $\Delta_{LP} \simeq -0.05$ meV. Due to the low count rate at this power, the integration time for this single data point was 96 hours. The result from our polariton-model simulations with $\hbar\omega_{NL} = 0.018$ meV is shown as continuous orange line.

The loss of antibunching statistics with higher excitation power is in line with the theoretical prediction of Verger *et al.*¹, and coincides with the results presented by Delteil *et al.*¹⁴, with their data following a very similar trend to the one observed here.

REFERENCES

- ¹A. Verger, C. Ciuti, and I. Carusotto, Phys. Rev. B **73**, 193306 (2006).
- ²C. Ciuti, P. Schwendimann, and A. Quattropani, Semicond. Sci. Technol **18**, S279 (2003).
- ³A. Reinhard, T. Volz, M. Winger, A. Badolato, K. J. Hennessy, E. L. Hu, and A. Imamoglu, Nature Photon. **6**, 93 (2012).
- ⁴C. Ciuti, V. Savona, C. Piermarocchi, A. Quattropani, and P. Schwendimann, Phys. Rev. B **58**, 7926 (1998).
- ⁵F. Tassone and Y. Yamamoto, Phys. Rev. B **59**, 10830 (1999).
- ⁶T. Fink, A. Schade, S. Höfling, C. Schneider, and A. Imamoglu, Nat. Phys. **First Online**, **11.12.2017** (2017).
- ⁷B. Deveaud, L. Kappei, J. Berney, F. Morier-Genoud, M. Portella-Oberli, J. Szczytko, and C. Piermarocchi, Chem. Phys. **318**, 104 (2005).
- ⁸S. Klembt, P. Stepanov, T. Klein, A. Minguzzi, and M. Richard, Phys Rev Lett **120**, 035301 (2018).
- ⁹B. Sermage, S. Long, I. Abram, J. Y. Marzin, J. Bloch, R. Planel, and V. Thierry-Mieg, Phys. Rev. B **53**, 16516 (1996).
- ¹⁰G. Muñoz-Matutano, D. Barrera, C. Fernández-Pousa, R. Chulia-Jordan, L. Seravalli, G. Trevisi, P. Frigeri, S. Sales, and J. Martínez-Pastor, Scientific Reports **6**, 27214 (2016).
- ¹¹S. Gehrsitz, F. K. Reinhart, C. Gourgon, N. Herres, A. Vonlanthen, and H. Sigg, Journal of Applied Physics **87**, 7825 (2000).
- ¹²T. J. Bright, J. I. Watjen, Z. M. Zhang, C. Muratore, A. A. Voevodin, D. I. Koukis, D. B. Tanner, and D. J. Arenas, Journal of Applied Physics **114**, 083515 (2013).

- ¹³L. Gao, F. Lemarchand, and M. Lequime, *Journal of the European Optical Society - Rapid publications* **8** (2013), ISSN 1990-2573.
- ¹⁴A. Delteil, T. Fink, A. Schade, S. Hofling, C. Schneider, and A. Imamoğlu, arXiv: 1805.04020 [cond-mat.mes-hall] (2018).